Pectoral Fin Flapping With and Without Deformations in the Bird Wrasse; 3-D Unsteady Computations

William C. Sandberg and Ravi Ramamurti
Laboratory for Computational Physics and Fluid Dynamics
Naval Research Laboratory
Washington, DC 20375-5344
USA

Rainald Löhner
Computational Sciences and Informatics Department
George Mason University
Fairfax, VA

Jeffrey A. Walker
Department of Biological Sciences
University of Southern Maine
Portland, ME 04103
USA

Mark M. Westneat
Department of Zoology
Field Museum of Natural History
Chicago,IL 60605-2496
USA

Abstract

The first three-dimensional unsteady computations of fish swimming with oscillating and deforming fins have been carried out (Ramamurti *et al, 2001).* The primary objective of these computations was to investigate the fluid dynamics of force production associated with the flapping aquatic flight of the bird wrasse. Experimental investigations have already been carried out on the bird wrasse during pectoral fin locomotion (Walker & Westneat, 1997). In the experimental studies the activity of the major muscles that power pectoral fin swimming, electromyographic activity, and pectoral fin kinematics were measured and the swimming performance was associated with the measured fin kinematics. We have, in the present computational work, taken the geometry of the wrasse and its pectoral fin, and fin kinematics data as the starting point for the computational investigation of the 3-D unsteady fluid dynamics. We have initiated the computational study by carrying out a 3-D steady computation and a complete set of 3-D quasi-steady computations for a range of pectoral fin positions and surface velocities. This paper reports on the results of the unsteady computations for pectoral fin oscillation with changing fin shape and with a non-deforming fin shape and compares these results to the experimental data and also compares the

results to quasi-steady and steady computational results (Sandberg & Ramamurti, 2000).

An unstructured grid-based unsteady Navier-Stokes solver with automatic adaptive remeshing was used to compute the flow about the wrasse through several complete cycles of pectoral fin oscillation. The shape deformation of the pectoral fin throughout the oscillation was taken from the experimental kinematics The pressure distribution on the body of the bird wrasse and on its pectoral fins was computed and integrated to give body and fin forces. The forces are decomposed into lift and thrust. The velocity field variation on the surface of the wrasse body, on the pectoral fins, and in the near-wake throughout the swimming cycle was computed. We compared our computational results for the steady, quasi-steady, and unsteady cases with the experimental data on axial and vertical acceleration obtained from the pectoral fin kinematics experiments.

Introduction

Many tropical reef fishes, including the Indo-Pacific reef fish, *Gomphosus varius*, or bird wrasse, fly underwater by flapping their pectoral fins with a motion that resembles the wing kinematics of several flying insects, including the hawkmoth, *Manduca sexta* (Walker & Westneat, 1997). Walker & Westneat (2000) argued this flapping motion is more mechanically efficient than the fore-aft rowing or paddling motion that is more typical in fishes. Indeed, wrasses with flapping strokes can achieve and maintain higher pectoral-fin powered swimming speeds than wrasses with rowing strokes (Walker & Westneat 2001).

The ease of working with fish make the bird wrasse a good model for investigating flapping flight mechanisms at moderate to high forward speeds. By contrast, previous works on the hawkmoth and the fruit fly, *Drosophila melanogaster*, have concentrated on hovering animals (Dickinson and Götz, 1996; Dickinson *et al.*, 1999; Ellington *et al.*, 1996; Willmott *et al.*, 1997, Ramamurti and Sandberg, 2001). The ability of animals to exploit previously shed vortices (Dickinson *et al.*, 1999) may depend on forward speed relative to oscillation frequency. The primary objectives in this work, were to (1) investigate the fluid dynamics underlying the generation of forces during pectoral fin oscillation with fin deformation in the bird wrasse, (2) use the fluid dynamic information to gain insight into the bird wrasse's impressive swimming capabilities, (3) to compare the fluid dynamics of a flapping appendage during forward motion with a flapping appendage during hovering, and (4) to compare the force generation capabilities of a fixed shape pectoral fin to those generated by the deforming fin .

For the first demonstration of a 3-D unsteady computation for fish fin motion and deforming body several years ago (Ramamurti and Sandberg, 1997), we chose the bluefin tuna. The tuna was selected since we wanted to examine thrust generation in a thunniform swimmer that generates its propulsive power primarily through caudal fin movement. It also seemed that a tuna was a reasonable first approximation to start with to investigate afterbody control surface dynamics for undersea

vehicles. We continue, in this investigation on *Gomphosus varius*, to focus on oscillating control surface flows for non-undulating bodies. As opposed to the tuna, where there is some afterbody undulation, body undulation is totally absent in the wrasse, except for those cases where fatigue sets in and a thrust assist from the body and caudal fin is occasionally provided. These cases, however, were excluded from the experimental analysis. The wrasse is thus an excellent candidate for a biologically inspired control surface design investigation. Since one of our interests is control surface design, we also examine the importance of fin deformation for force generation throughout the stroke cycle.

The Incompressible Flow Solver

The governing equations employed are the incompressible Navier-Stokes equations in Arbitrary Lagrangian-Eulerian (ALE) formulation which are written as

$$\frac{\partial \mathbf{v}}{\partial t} + \mathbf{v}_a \cdot \nabla \mathbf{v} + \nabla p = \nabla \cdot \sigma, \qquad (1)$$

$$\nabla \cdot \mathbf{v} = 0, \qquad (2)$$

where p denotes the pressure, $\mathbf{v}_a = \mathbf{v} - \mathbf{w}$ the advective velocity vector (flow velocity $\mathbf{v}$ minus mesh velocity w) and both the pressure p and the stress tensor σ have been normalized by the (constant) density ρ, are discretized in time using an implicit time stepping procedure. Thus the equations are Eulerian for zero mesh velocity and Lagrangian if the mesh velocity is the same as the flow velocity. The present time-accurate flow solver is discretized in space using a Galerkin procedure with linear tetrahedral elements. The details of the flow solver have already been discussed extensively elsewhere (Ramamurti *et. al.* 1992, 1994, 1995 1997) in connection with succesfully validated solutions for numerous 2-D and 3-D, laminar and turbulent, steady and unsteady flow problems.

Unstructured Mesh Generation and Adaptive Re-meshing

In order to carry out computations of the flow about oscillating and deforming geometries which may be quite complex, several pieces of grid technology are needed. First, one must be able to rapidly generate a surface triangulation. If many complex surfaces are intersecting, and they are discrete components as is the case for multiple fins on a fish body, a capability to construct the total surface mesh including the intersection loci automatically, is essential. One then needs to describe the mesh motion on the moving surface, couple the moving surface mesh to the volume grid in a smoothly varying manner, and describe the dynamic remeshing of the volume grid in proximity to the moving surface as the surface moves and deforms. In deformations, the surface motion may be severe, leading, in the absence of remeshing, to distorted elements which in turn lead to poor numerical results. If the bodies in the flow field undergo arbitrary movement, a fixed mesh structure will lead to badly distorted elements. This means that at least a partial regeneration of the computational domain is required. On the other hand, if the bodies move through the flow field, the positions of relevant flow features will change. Therefore, in most of the computational domain a new mesh distribution will be required.

One approach to solve these problems is to add several layers around the moving bodies that move rigidly with the body. As the elements (or edges) move, their geometric parameters (shape-function derivatives, jacobians, etc.) need to be recomputed every timestep. If the whole mesh is assumed to be in motion, then these geometric parameters need to be recomputed globally. In order to reduce the number of global remeshings and hence save CPU-time when using this approach, only a small number of elements surrounding the bodies are actually moved. The remainder of the field is then treated in the usual Eulerian frame of reference, avoiding the need to recompute geometric parameters. We refer the reader to earlier papers (Löhner *et al.*, Shostko *et al.* 1999) which discuss the mathematics and numerics of the unstructured grid generation and adaptive remeshing codes used in this work.

3-D Wrasse Body and Pectoral Fin Description

To get the 3-D surface coordinates of a bird wrasse, a 21 cm standard length individual was frozen and sliced into nine transverse sections. Section outlines were digitized using a modification of the public domain NIH Image program (developed at the U.S. National Institutes of Health and available on the Internet at http://rsb.info.nih.gov/nih-image/) for the Apple Macintosh (the modification is available from J.A. Walker upon request). The outline coordinates were used to generate a smooth surface using standard cubic spline methods.

While the digitized individual is representative of the geometry of the subjects from the experiment (Walker & Westneat, 1997), it was not one of the experimental subjects. The exact geometry and the corresponding surface mesh of the bird wrasse for which the computations have been carried out is shown in Figure 1.

Pectoral Fin Kinematics Data

Pectoral fin surface coordinates were estimated from the experimental data. In the original experiment, five aluminum markers were attached to one of the pectoral fins; two on the leading edge, two on the trailing edge, and one on the fin tip. Fin motion was filmed using S-VHS video at 60 Hz. The five fin markers and the dorsal base of the pectoral fin were digitized from both lateral and dorsal views. The three-dimensional coordinates of the markers throughout the cycles were obtained from the marker positions in the two views. For the present analysis, the motion of the three distal edge markers was smoothed with a quintic spline function (Walker, 1998). In order to remove the kink in the distal (tip) edge of the fin that necessarily resulted from only three digitized points, a smooth curve was fit to the distal edge by increasing the number of points to fourteen (the number of fin rays in the fin) using linear interpolation and smoothing the distal edge with a quintic spline function (Walker, 1998). 3-D surface coordinates were obtained by linear interpolation between the digitized pectoral fin base of the representative individual, scaled to the size of an experimental individual, and the distal edge of an experimental individual.

Walker and Westneat (1997) observed that the fins flapped synchronously during rectilinear motion at all test speeds. They also noted that *G. varius* flapped its pectoral fins up and down with a small anterior movement during abduction and a small posterior movement during adduction. Flapping frequency was seen to increase linearly with speed. The mean flapping frequency was 2.9 Hz at 22cm/sec and 4.2Hz at 50 cm/sec. In the computations carried out here we used a pectoral fin oscillation frequency of 3.3 Hz. corresponding to a swimming speed of approximately 45 cm/sec (2L/sec.). The digitized positions of the five markers throughout the oscillation cycle served to specify the kinematics of the pectoral fin for the present computations. Photographs showing dorsal and ventral views of fin geometry at two extended positions during the cycle are shown in Figure 2.

Computational Results

A set of steady computations and a set of quasi-steady computations were carried out at selected times during the fin oscillation cycle. The positions of the pectoral fin at selected times during both abduction (downstroke) and adduction (upstroke), shown in Figure 3, were chosen for the quasi-steady computations. To simulate the quasi-steady state solution at any instant of time, the velocity of the fin was obtained from the experimental kinematics data at that instant. This velocity was then used as the mesh velocity at the fin surface, without actually moving the fin surface. The computed flow solution is thus the steady state flow with the high velocity motion of the fin superimposed on it.

Forces on the pectoral fin and the fish body were computed, for the quasi-steady simulation, for each orientation of the fin by integrating the surface pressures. The computed force on the fin was non-dimensionalized by the dynamic head due to mean tip velocity of the fin as follows:

$$C_F = \frac{F}{1/2\rho V^2}, \qquad V = 2\phi Rn \tag{3}$$

Here, ϕ is the stroke amplitude in radians, R is the maximum fin radius and n is the frequency of the fin oscillation in Hz.

A complete discussion of the steady flow computational results and a comparison of them with the quasi-steady flow computational results has been presented elsewhere (Sandberg *et al.*, 2000). For completeness, and to demonstrate the inadequacy of steady and quasi-steady flow computations for this problem, the computed steady forces are compared with those for the quasi-steady and unsteady computations later in this paper.

Unsteady Computations

Unsteady computations were also carried out using the prescribed fin kinematics. A new mesh movement capability to accommodate the deforming fin surface was developed and added to the mesh movement algorithm used in earlier flapping fin computations (Ramamurti & Sandberg, 2000, 2001). The motion of the fin surface was first prescribed at a finite set of control points. The Cartesian coordinates on the fin surface were then transformed to a parametric space. The coordinates of the surface points were maintained to be constant in the parametric space throughout the

computation while the Cartesian coordinates were computed according to the prescribed motion of the control points.

Unsteady simulations were carried out with the bird-wrasse swimming at 45 cm/s. The stroke amplitude is approximately 2.14 radians and the frequency of fin oscillation is 3.3 Hz, resulting in a mean tip speed of approximately 50 cm/s. The computation was carried out for more than 4 cycles of fin oscillation using a computational mesh consisting of approximately 150K points and 840K tetrahedral elements.

At the beginning of the downstroke the fin is quite close to the body and it is difficult to clearly visualize the fin flow field, hence these time steps have not been included for visualization. The simulation of the pectoral fin motion was actually begun slightly after the start of the downstroke, at t =0.05 sec., rather than at t =0.0, to avoid the difficulties associated with contact of the fin and the body surfaces. This is considered to have almost no influence on the magnitude of the forces since the force production by the fin at that time is negligible.

The velocity vectors on the entire wrasse and its pectoral fin are shown in Figure 4. The body flow at this instant is typical of that observed throughout the stroke cycle. The flow over most of the wrasse body is observed to be uniform throughout the stroke cycle, with the lowest velocities occurring on the ventral side of the forebody and afterbody. The highest velocities are observed on the pectoral fin, above the root of the fin, and on the dorsal side just anterior to the caudal fin.

A closer view of the pectoral fin flow is given in Figures 5 through 7 at critical times during the cycle. Figure 5 shows the velocity vectors on the pectoral fin at t = 1.0568 sec., which occurs at about 78% through the downstroke. This is the time of maximum force production on the downstroke. A clockwise flow is seen at the root above the leading edge. The stagnation zone is seen under the leading edge at the root with the velocity increasing outward, dominated by the axial (leading edge-to-trailing edge) component of flow. Figure 6 shows the velocity vectors occurring at t = 1.1021 sec. which corresponds to about the beginning of the upstroke. We observe that despite the counterclockwise flow on the upper surface behind the leading edge near the fin root, the clockwise flow on the wrasse body above the root remains. Figure 7 corresponds to the time of highest force production during the upstroke. The flow at the root is quite complex, showing a saddle point type of flow induced on the body by the combined upward motion of the fin and the axial inflow. Very high magnitudes of vertically directed flow are seen in two zones on the surface of the fin, at the tip region and in the high gradient zone approaching the fin root.

In order to provide additional information on the flow about the fin during times of high force production we also looked at the velocity off the fin surface in several chordwise planes, moving from near the root toward the fin tip. Figures 8a and b show that there is only a small outwardly induced flow (root-to-tip) during the downstroke, and a small inwardly induced flow during the upstroke. The magnitude of the spanwise component of the flow observed in Fig. 8a and 8b is in the range of 10-15 cm/sec

and is only seen in the plane 1.5 cm from the fin root. As an additional diagnostic for the flow at the leading edge we plot, in Figures 9a and 9b, the iso-contours of the z-component (directed from root to tip) of vorticity. We observe that there is no indication of a strong spanwise vorticity component on the upper surface of the pectoral fin which would exist if a leading-edge spiral vortex was present. This can be seen in Figure 10 where particle traces show primarily chordwise motion, except in the tip vortex region. A leading-edge spiral vortex with spanwise flow has been seen on the upper surface of the wing by Ellington *et al*. (1996) in their wind-tunnel experiments on tethered hawkmoths. A spanwise flow in the vortex core has been proposed as the mechanism for stabilization of the leading edge vortex on the hawkmoth. It is interesting to note that our flapping wing computations for the *Drosophila melangaster*, (Ramamurti *et al.*, 2001), (the forces computed are seen in Figures 11a and b to be in good agreement with the experimental data), also showed no evidence of a spiral leading-edge spanwise vortex on the upper surface of the wing. What was observed was a counterclockwise vortex on the pressure side of the wing during both upstroke and downstroke. The absence of a leading edge spiral vortex on the wrasse pectoral fin suggests that the dynamics of force generation in the wrasse pectoral fin swimming is different than the fluid dynamics of force production in the hovering hawkmoth. In our case we clearly are, as can be seen from the surface velocity vectors, particle traces, and iso-vorticity contours, more dominated by the axial flow than is the case for the hovering hawkmoth.

Figures 12 and 13 show the results of the steady state and quasi-steady state computations. The time-varying 3-D lift and thrust forces, shown in Figures 14 and 15, were computed by integrating the surface pressure over the wrasse body and fin at each time step throughout the simulation. The striking difference between the unsteady lift and thrust forces and those from our steady and quasi-steady computations is that the computed forces are much larger in magnitude in the unsteady computations.

We also computed the fore-aft and dorso-ventral accelerations of the fish, assuming a mass of 100g, from the thrust and lift forces. We compare our computed accelerations, shown in Figures 15 and 16, with the experimentally derived fore-aft acceleration results for the 47 cm/sec data from Figure 5a of (Walker &Westneat, 1997). We find the computational results to be in good agreement with the data from the swimming experiments. The principal observations from the comparison between the computed results and those from the experiments are presented below.

We consider first the axial forces and accelerations. Experimentally for the 47 cm/sec data set, an aft acceleration is observed throughout the downstroke. The maximum value of the aft acceleration, which ranges between 20-45 cm/sec^2, occurs during the first quarter of the downstroke and again near the three-quarters region of the downstroke. The aft acceleration decreases to approximately zero near mid-stroke and at the end of the downstroke. The acceleration data for the other swimming speeds all show a

small acceleration which starts as aft directed, changes sign but has a small magnitude, and then becomes aft directed for the remainder of the downstroke. The computational results are presented in Fig. 16.

The axial acceleration starts near zero as the downstroke begins and increases to a maximum at about 30% of the downstroke. It then decreases, going through zero acceleration to an aft–directed acceleration for the remainder of the downstroke. The maximum aft-directed acceleration occurs at about 90% through the downstroke, in excellent agreement with the data. The small forward directed acceleration peak we observe from the computations is not present in the data. If one adds the viscous body and fin drag to our computed drag values, all of our positive accelerations will be reduced and the aft-directed accelerations will be increased. A conservative estimate of the body and fin viscous drag throughout the swimming cycle can be made by carrying out a Navier-Stokes drag computation for the fully-extended fin case. The Reynolds number for this simulation is set to be approximately 16,000 based on the pectoral fin length and a fish swimming speed of 45 cm/s. The configuration that was considered is the fully extended pectoral fin, which corresponds to an instant during the middle of the downstroke. We have done this computation and find a body viscous drag of 1.05Kdynes and a fin viscous drag of 2.20Kdynes. This corresponds to an aft-directed axial acceleration, for the 100g fish, of 32.5 cm/sec^2, which exceeds the magnitude of the positive peak. One cannot, however, subtract this value from any points on the acceleration curve since it is a steady result and thus, strictly speaking, cannot be used to alter the computed unsteady results. It does however serve to indicate that at some point during both the upstroke and the downstroke, a viscous drag force of approximately this magnitude would be experienced by the wrasse. Therefore it also indicates that if an unsteady Navier-Stokes computation were performed one would have a substantially lower positive region, or possibly no positive region, during the downstroke.

Comparing our computed results for fore-aft acceleration during the upstroke with the experimental results we find good agreement. The experiments show an increase in foreward acceleration to a maximum occuring between 40-50% of the upstroke then decreasing steadily to zero at about 90% of the upstroke. The maximum accelerations from the experiments were in the range of 30-90 cm/sec^2. We obtain a forward acceleration maximum of about 45 cm/sec^2 at approximately 60% of the upstroke with the acceleration then steadily steeply toward zero for the beginning of the downstroke.

We also compare our computed results for lift force, Fig. 15, with the dorso-ventral acceleration from Figure 5b of (Walker and Westneat, 1997). The distributions of accelerations for fishes swimming at 47 cm/sec rise from a negative value at the start of abduction (downstroke) to a maximum dorsal acceleration at about 44% abduction, decreasing to zero at about 80% and becoming negative through the remainder of the downstroke. The range of the maximum dorsal acceleration is from 70 to 100 cm/sec^2. The range of the ventral accelerations at the start of

abduction is from 10-30 cm/sec^2. Our computed results show a ventral (downward) acceleration at the start of the downstroke, rising to a maximum dorsal acceleration at about 40% abduction and then decreasing to zero at about 70% abduction and steadily becoming negative. The magnitude of the computed dorsal acceleration is approximately 80 cm/sec^2. The value of the ventral acceleration at the start of abduction is approximately 40 cm/sec^2. Again there is excellent agreement with the experimental results.

It should also be noted here that the mass of the fish we have used in our computations, 100 grams, was not a mass of any of the fish population making up the 47cm/sec data. The masses of the fish making up the 47cm/sec data ranged between 24 and 50 grams. Hence, we are not actually comparing our computations against the data for any specific fish in the original experiments, but rather we are demonstrating that our computed fish dynamics are representative of the dynamics observed experimentally for the bird wrasse as a species.

The computed thrust force is non-dimensionalized by the dynamic head using Eq. 3. Figure 15 shows the variation of the thrust coefficient in time. Looking now at the lift and thrust forces computed from the quasi-steady state simulations, Fig. 7, we have a trend similar to that for the unsteady forces, but the magnitude of the computed forces are much smaller; the peak thrust coefficient from the quasi-steady computations is 0.5 compared to 2.0 in the unsteady computations. The unsteady lift coefficients vary between +4.0 and –4.0 while those for the quasi-steady computation range between +0.3 to –0.6. Since the unsteady computations are in good agreement with the results from the swimming experiments we conclude that 3-D inertial effects, ignored in the quasi-steady computations, are quite significant in the thrust and lift generation processes.

Effect of Rigid Fin

In order to study the effect of spanwise variation of camber of the fin on the propulsion, we modified the fin to be rigid. This is done by selecting the two fin root locations and the fin leading edge tip location at t= 0.15sec. The fin is then formed as a planar surface with the three points. This rigid fin was then moved according to the prescribed fin tip movement. Figure 17a shows the variation of the thrust coefficient for the flexible fin compared to the rigid fin with a fish swimming velocity of 45cm/s. The peak in the thrust coefficient during the upstroke occurs at almost the same instant in time albeit the magnitude is reduced by a factor of 2. The rigid fin case showed a prominent loss of lift in the upstroke as shown in Fig. 17b. The dynamics of the thrust production during the downstroke is quite different from the flexible fin case, especially in the beginning of the stroke. This may be due to the change in angle of attack of the leading edge of the fin that is important to capture the rotational effect of the fin.

In earlier simulations of the flow over a hovering fruit-fly *Drosophila*, it was found that the rotational mechanism was responsible for increase in thrust at the beginning of the downstroke. Therefore, the presence of large swimming velocity could advect the vortices left by the fin

downstream and result in the loss of thrust. Hence, the swimming velocity of the fish was reduced to understand its effect on the thrust production during the beginning of the downstroke. The swimming velocity of the fish was reduced to 20cm/s. Figure 2 shows the effect of this change on the thrust and lift coefficients and it is minimal.

Summary and Conclusions

We have computed the unsteady dynamics about a bird wrasse with flapping and deforming pectoral fins using a new moving mesh capability for unstructured adaptive meshes. The unsteady computations have been compared with steady state computations, quasi-steady state computations, and experimental results. We have found that the steady state computations are incapable of describing the dynamics associated with the flapping fins. The quasi-steady state computations, with correct incorporation of the experimental kinematics, are useful in determining trends in force production. They do not, however, provide accurate estimates of the magnitudes of the forces produced. Completely unsteady computations about the deforming pectoral fins using experimentally measured fin kinematics are found to give excellent agreement both in the time history of force production throughout the flapping strokes and also the magnitudes of the generated forces. We have confirmed the experimental findings on the time of occurrence of the maximum thrust during adduction and the maximum lift during abduction. We have concluded that 3-D inertial effects are not a minor perturbation but are critical for accurate force computations. We have also observed, through flow visualization throughout the stroke cycle, only a very small flapping-induced inward and outward spanwise velocity, acting over the near-root region of the pectoral fin. We have not observed a spiral leading edge vortex on the pectoral fin. We find the pectoral fin flapping flow to be dominated by the strong axial flow as opposed to the flows in hovering insects such as the hawkmoth, where an attached leading edge spiral vortex has been shown to be of importance in high lift generation. In pectoral fin flapping associated with swimming against a strong current the primary need for the wrasse is to attain the axial acceleration neccesary for high speed forward motion, while some vertical position changes can be tolerated. It is possible that one might observe during low-speed maneuvering, where vertical position keeping is more important, wrasse pectoral fin flows more similar to those of the hawkmoth or *Drosophila*. Fin deformation during the stroke cycle was seen to be quite important, accounting for a two-fold increase in the magnitude of the maximum force generated and preventing a loss of lift during the upstroke.

References

Dewar, H. and Graham, J., Studies of (1994). Tropical Tuna Swimming in a Large Water Tunnel, III Kinematics, *J. Exp. Biol.*, **192**, 45-59.

Dickinson, M. H. and Götz, K. G. (1996). The wake dynamics and flight forces of the fruit fly *Drosophila melanogaster*. *J. Exp. Biol.* **199**, 2085-2104.

Dickinson, M. H., Lehmann, F.-O. and Sane, S. P. (1999). Wing rotation and the aerodynamic basis of insect flight. *Science* **284**, 1954-1960.

Ellington, C. P., Van den Berg, C. and Willmott, A. P. (1996). Leading-edge vortices in insect flight. *Nature* **384**, 626-630.

Ramamurti, R. and Löhner, R., (1992). Evaluation of an Incompressible Flow Solver Based on Simple Elements, *Advances in Finite Element Analysis in Fluid Dynamics*, FED **137**, Editors: Dhaubhadel, M. N. *et al*., ASME Publication, New York, 33-42.

Ramamurti, R. and Sandberg, W. C., (2001). A 3-D Computational Study of Aerodynamic Mechanisms of Insect Flight, submitted *J. Exp. Biol*.

Ramamurti, R. and Sandberg, W.C., (2001). Computational Study of 3-D Flapping Foil Flows, *AIAA-2001-0605*, Reno, NV.

Ramamurti, R., Löhner, R., and Sandberg, W. C., (1994). Evaluation of a Scalable 3-D Incompressible Finite Element Solver, *AIAA-94-0756*, Washington, DC.

Ramamurti, R., Löhner, R., and Sandberg, W. C., (1995). Simulation of a Torpedo Launch Using a 3-D Incompressible Finite Element Flow Solver, *AIAA-95-0086*, Washington, DC.

Ramamurti, R., Löhner, R., and Sandberg, W. C., (1999). Computation of the 3-D Unsteady Flow Past Deforming Geometries, *Int. J. Comp. Fluid Dyn.*, 13, 83-99.

Ramamurti, R., Sandberg, W. C., and Löhner, R., (1997). Computation of 3-D Unsteady Flow Past Deforming Geometries, *NRL Technical Memorandum Report*, NRL/TMR/6410-97-8101, October 20.

Ramamurti, R., Sandberg, W.C. and Löhner, R., (2000). Simulation of the Dynamics of Micro Air Vehicles, *AIAA-2000-0896*, Reno,NV.

Ramamurti, R., Sandberg, W.C. and Löhner, R., (2001). Simulation of Flow about Flapping Airfoils Using a Finite Element Incompressible Flow Solver, *AIAA J.*, **39**,2,253-260.

Sandberg, W. C., and Ramamurti, R., (1996). 3-D Unsteady Flow Past a Bluefin Tuna with Caudal Fin Oscillation, *Proc. DARPA Symposium on Drag Reduction in Biological Systems*, Johns Hopkins University, Baltimore, MD.

Sandberg, W. C., and Ramamurti, R., (1999). Unsteady Flow Computational Technology for Flapping Fins: A Status Report, *Proc. Unmanned Undersea Submersibles Technology Symposium*, Durham, NH.

Sandberg, W. C., Ramamurti, R., Westneat, M. W., and Walker, J. A., (2000). 3-D Computations of Flapping Aquatic Flight**,** *Proc. 1st Intl. Symp. On Aqua-Bio Mechanisms*, Honolulu, HI.

Shostko, A. A., Löhner, R., and Sandberg, W. C., (1999). Surface Triangulation Over Intersecting Geometries, *Int. J. Num. Meth. Engg.*, **44**, 1359-1376.

Walker, J. A. (1998). Estimating velocities and accelerations of animal locomotion: A simulation experiment comparing numerical differentation algorithms. *J. Exp. Biol.* **201**, 981-995.

Walker, J. A. and Westneat, M. W. (2000). Mechanical performance of aquatic rowing and flying. *Proc. R. Soc. Lond. B.* **267**, 1875-1881.

Walker, J. A. and Westneat, M. W. (2001). Performance limits of labriform propulsion: a comparison between rowers and flappers. *Submitted to J. Exp. Biol.*

Walker, J. A., and Westneat, M. W., (1997). Labriform Propulsion in Fishes: Kinematics of Flapping Aquatic Flight in the Bird Wrasse, *Gomphosus Varius.* (Labridae), *J. Exp. Biol.* **200**, 1549-1569.

Westneat, M. W., and Walker, J. A., (1997). Motor Patterns of Labriform Locomotion: Kinematic and Electromyographic Analysis of Pectoral Fin Swimming in the Labrid Fish *Gomphosus Varius*, *J. Exp. Biol.*, **200**, 1881-1893.

Willmott, A. P., Ellington, C. P. and Thomas, A. L. R. (1997). Flow visualization and unsteady aerodynamics in the flight of the hawkmoth, *Manduca sexta. Phil. Trans. R. Soc. Lond. B* **352**, 303-316.

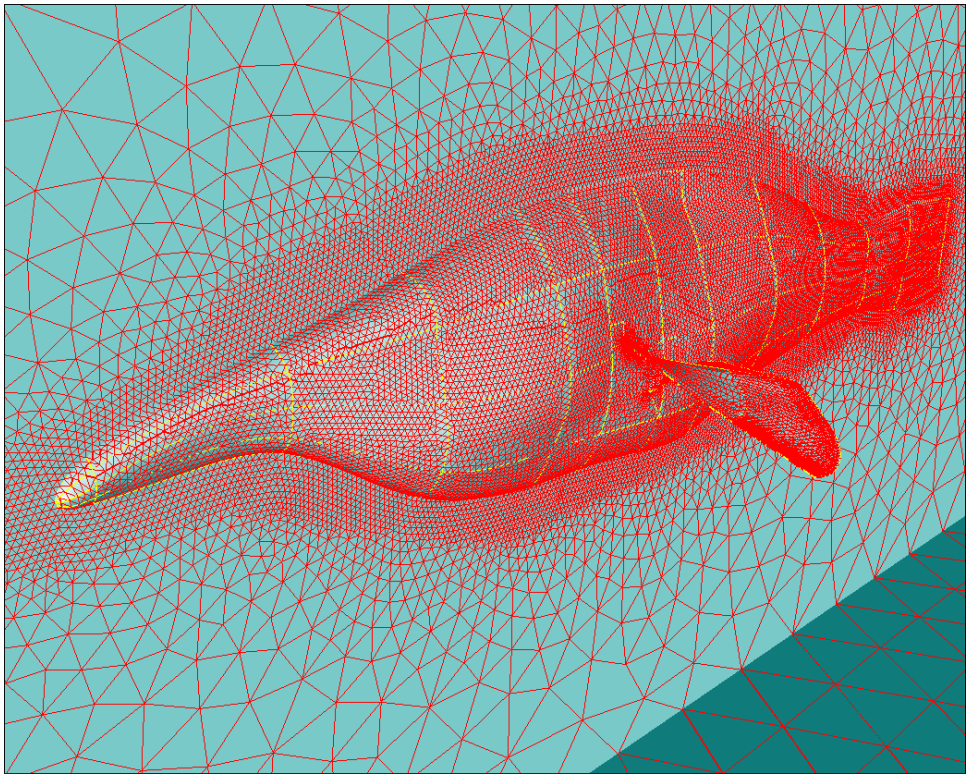

Figure 1. Computational Surface Mesh for Body and Pectoral Fin

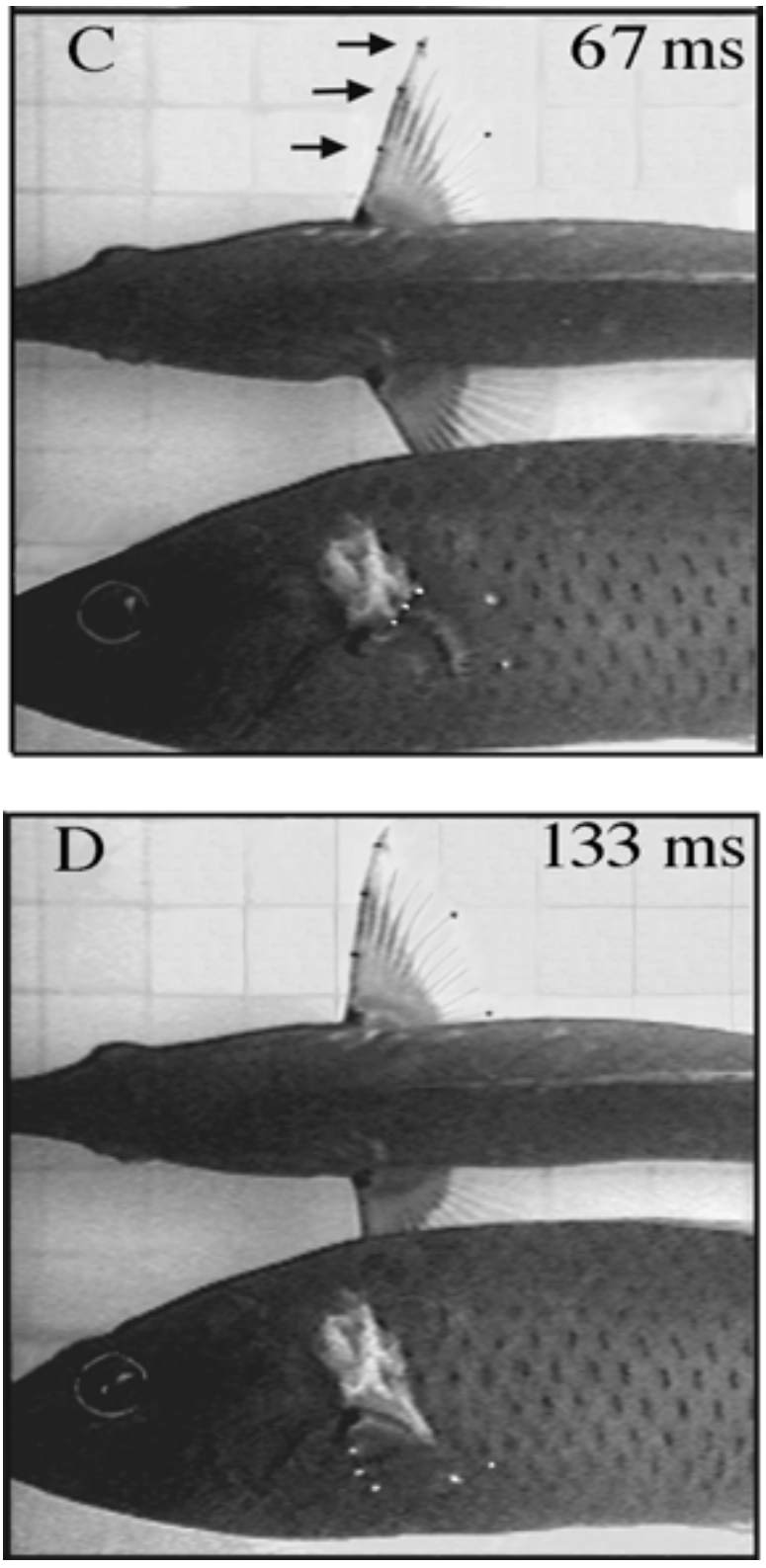

Figure 2. Pectoral Fin and Markers During mid-phase (C) and late phase of Downstroke (D).

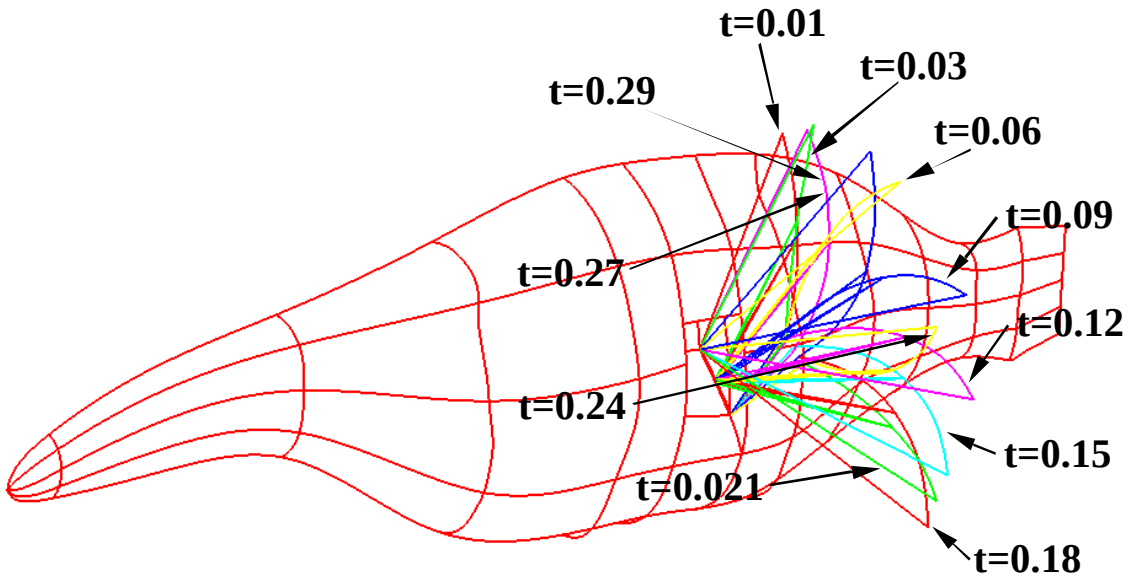

Figure 3. Pectoral fin location at various times throughout the stroke cycle.

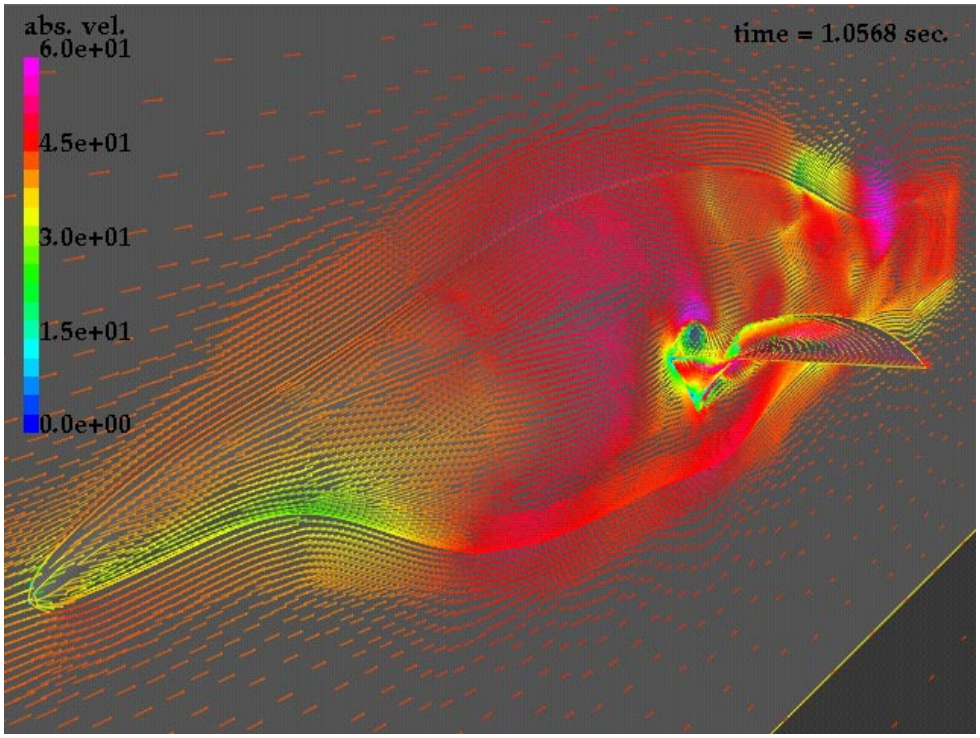

Figure 4. Velocity vectors on the surface of the Bird-Wrasse, t= 1.0568 sec.

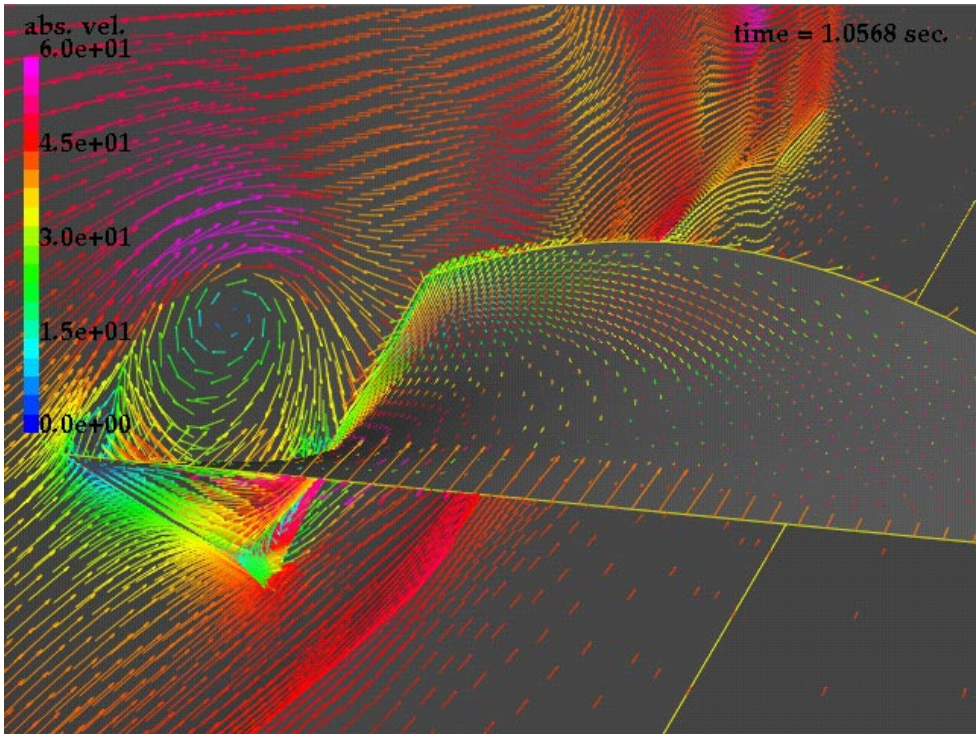

Figure 5. Velocity vectors on wrasse and pectoral fin
V=45 cm/s, t= 1.0568 sec.

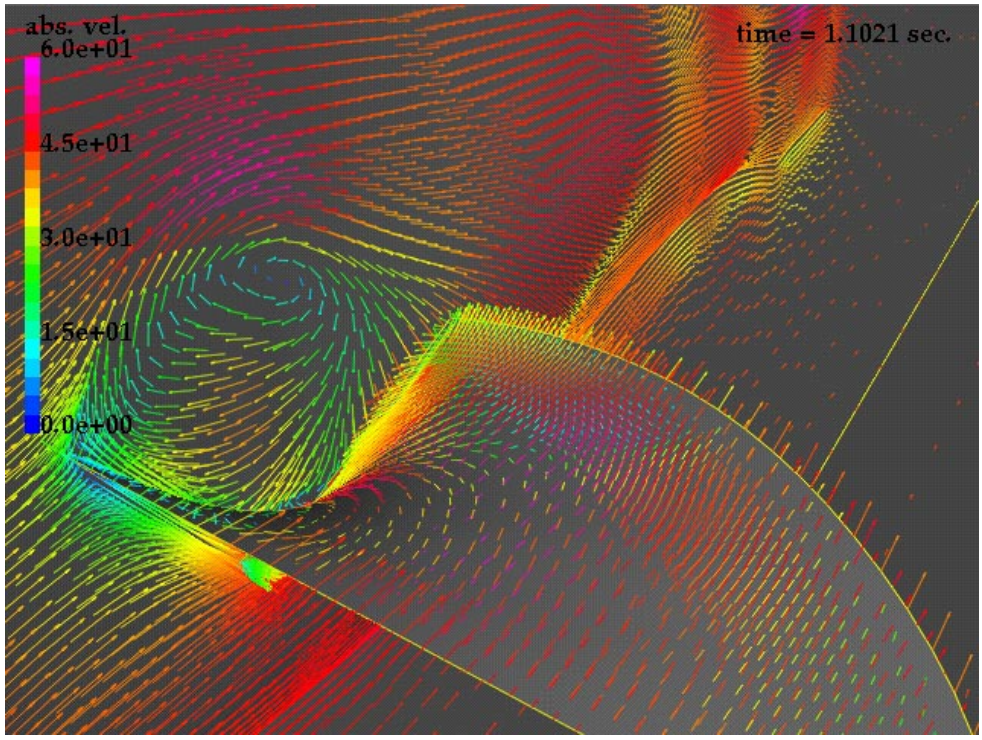

Figure 6. Velocity vectors on wrasse and pectoral fin, V=45 cm/sec, t= 1.1021 sec.

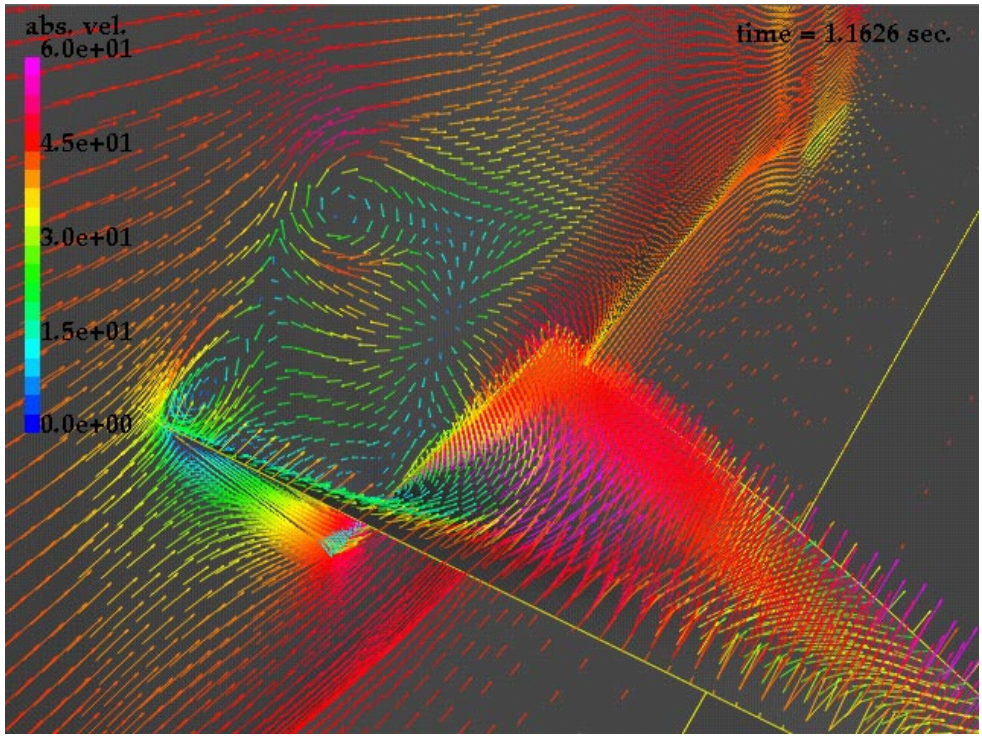

Figure. 7 Velocity vectors on wrasse and pectoral fin,V=45 cm/sec, t= 1.1626 sec.

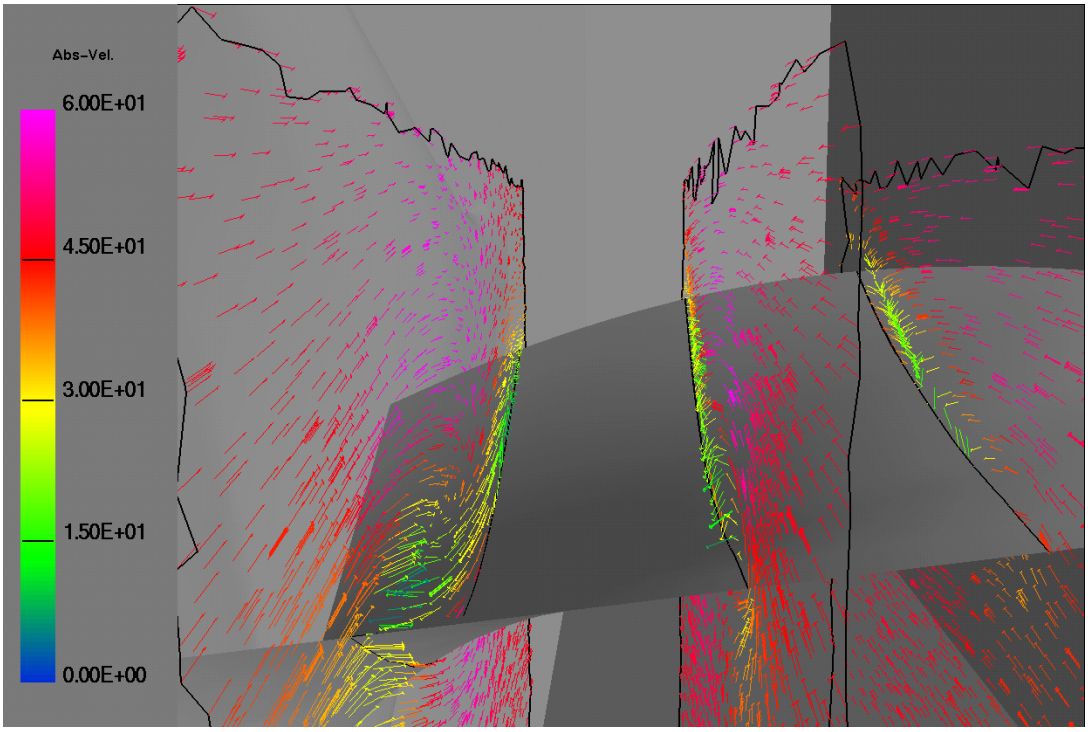

a. t = 1.0568 sec.

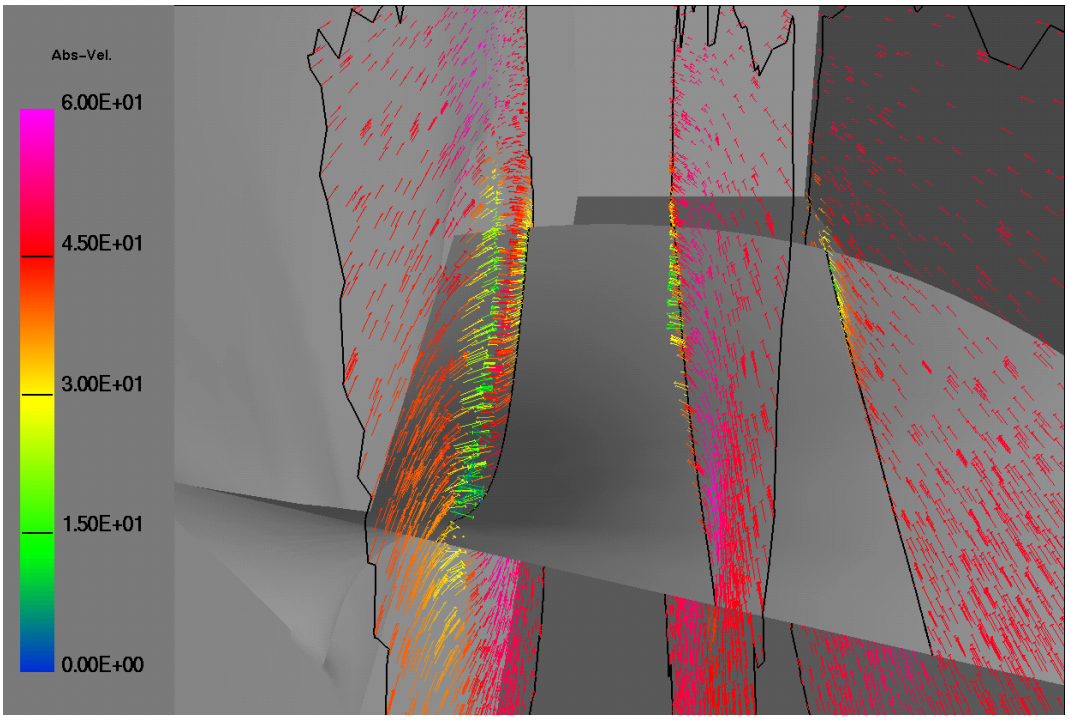

b. t = 1.1021 sec.

Figure 8. Velocity vectors along z = 1.5 cm, 2.0 cm and 2.5cm planes

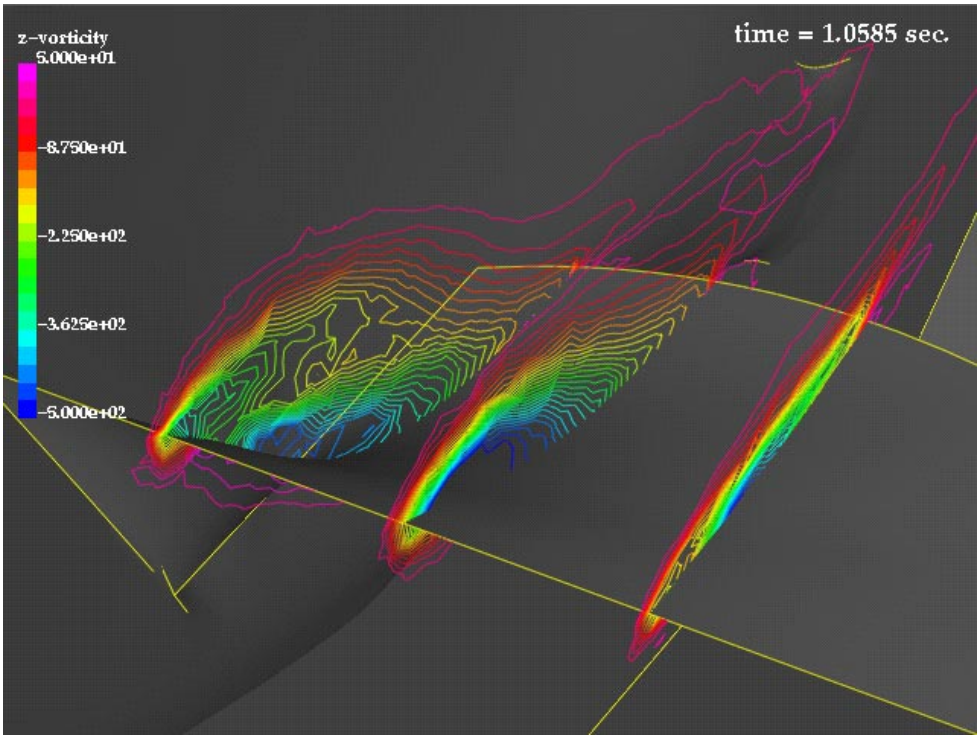

a. t = 1.0568 sec.

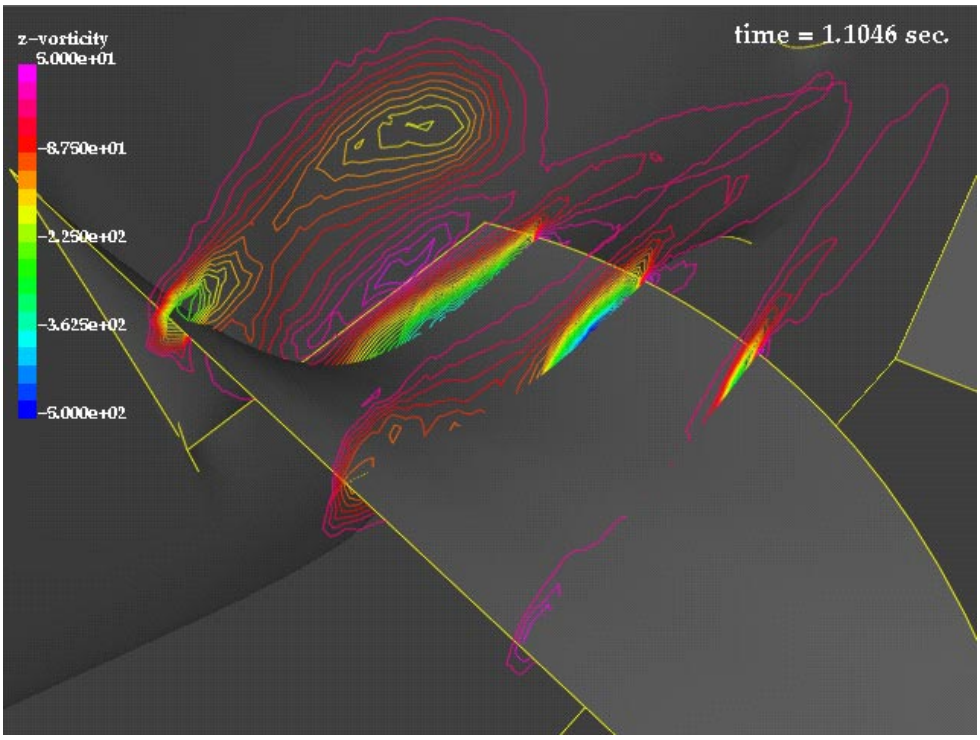

b. t = 1.1021 sec.

Figure 9. Spanwise variation of iso-contours of z-component of vorticity

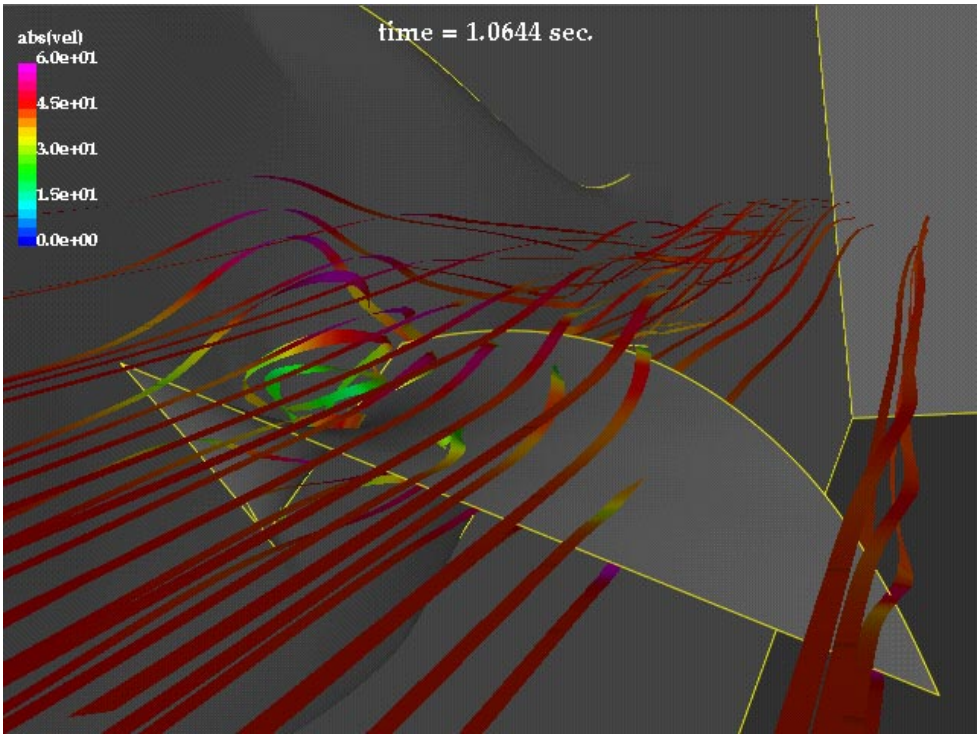

Figure 10. Particle traces over the pectoral fin, V = 45cm/sec, t = 1.0644 sec.

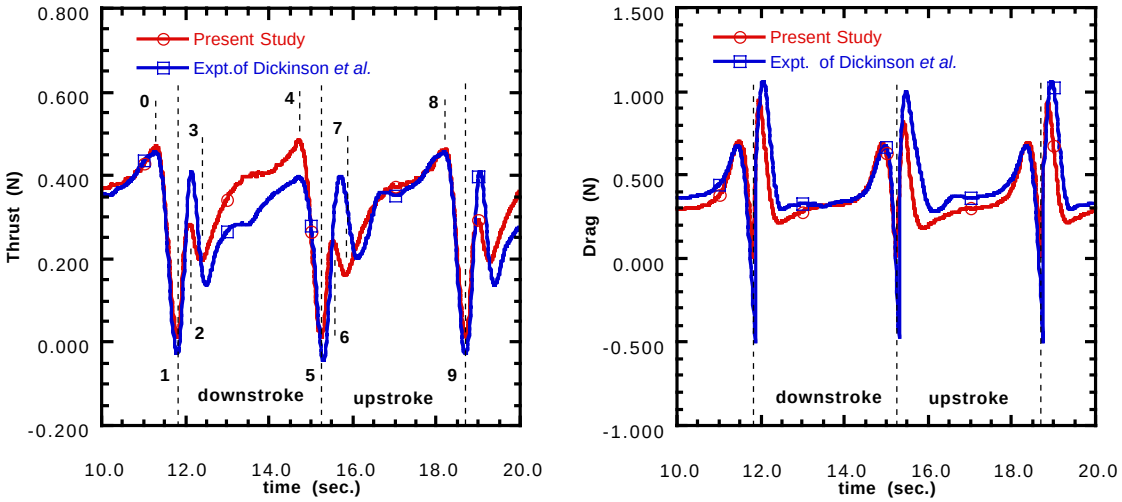

a. Thrust b. Drag

Figure 11. Comparison of time history of thrust and drag forces with experimental data from Dickinson *et al.*

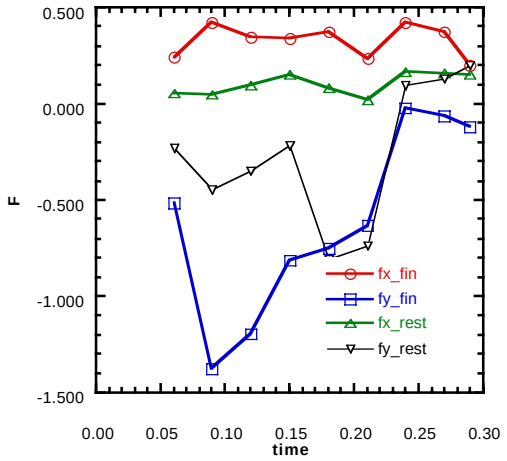

Figure 12. Variation of thrust and lift forces, steady state computations

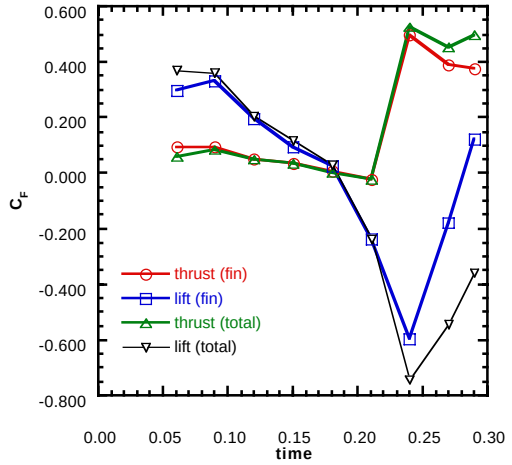

Figure 13. Variation of thrust and lift forces, quasi-steady state computations

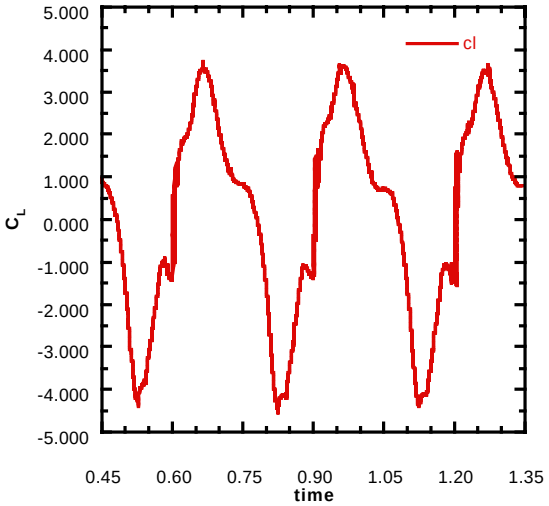

Figure 14. Time Variation of Unsteady Lift Forces

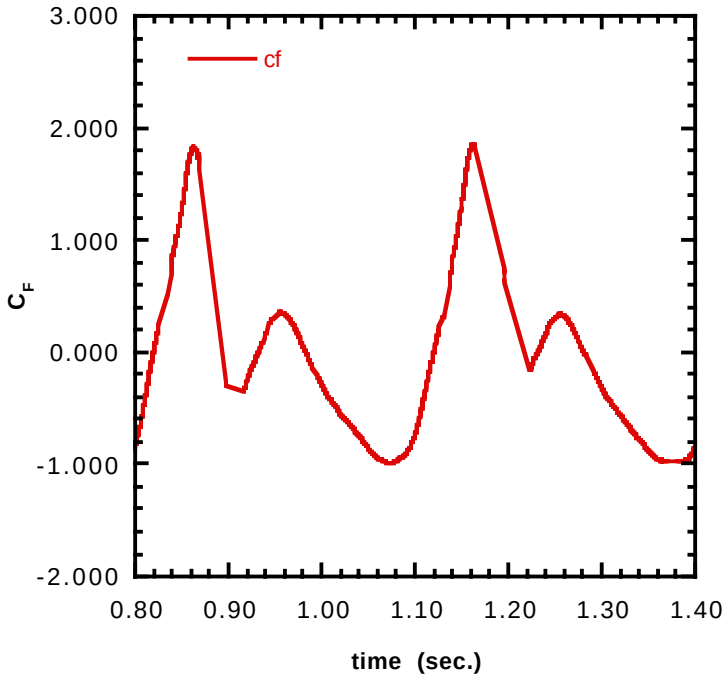

Figure 15. Time Variation of Unsteady Thrust Forces

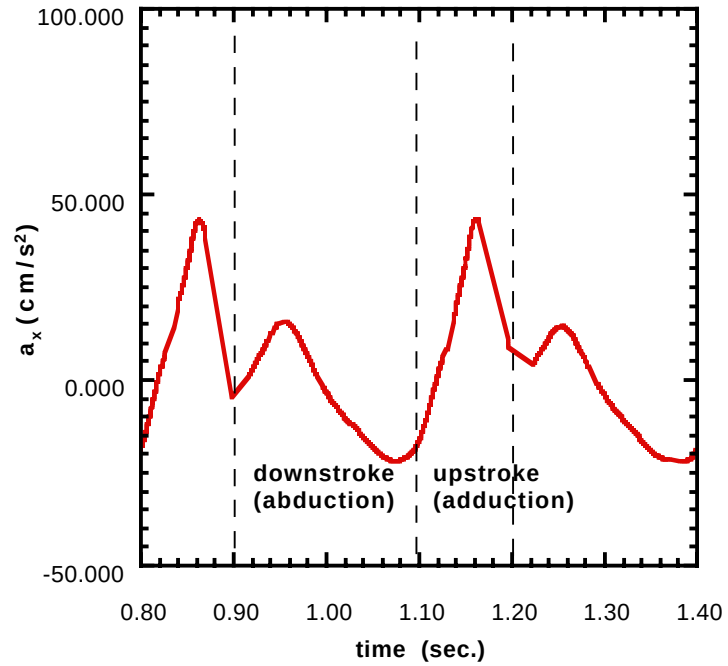

Figure 16. Time Variation of Fore-Aft Acceleration

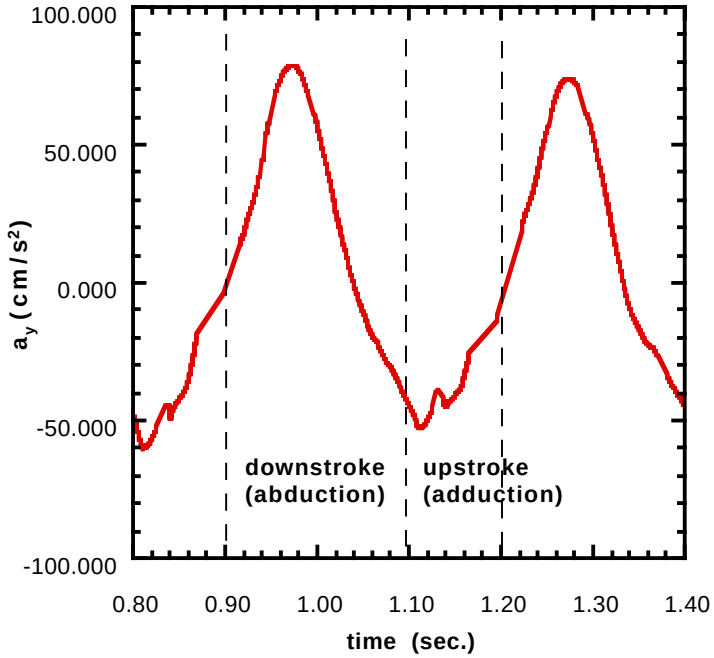

Figure 17. Time Variation of Dorsal-Ventral Acceleration

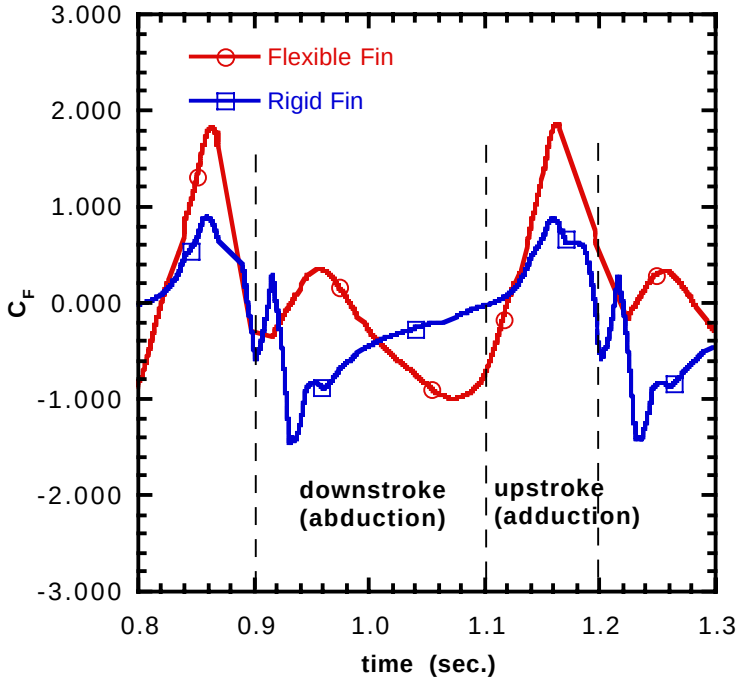

a. coefficient of thrust

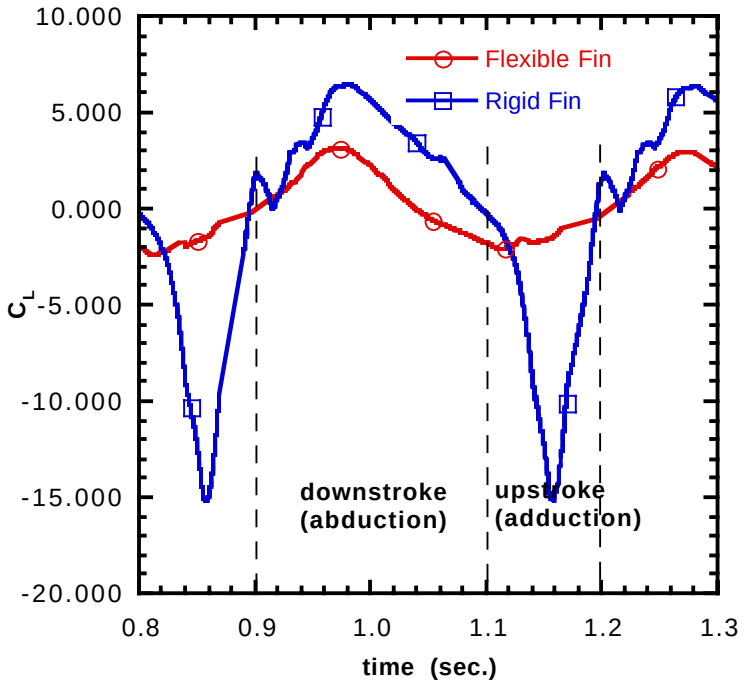

b. coefficient of lift

Figure 18. Effect of rigid fin, V = 45cm/sec.

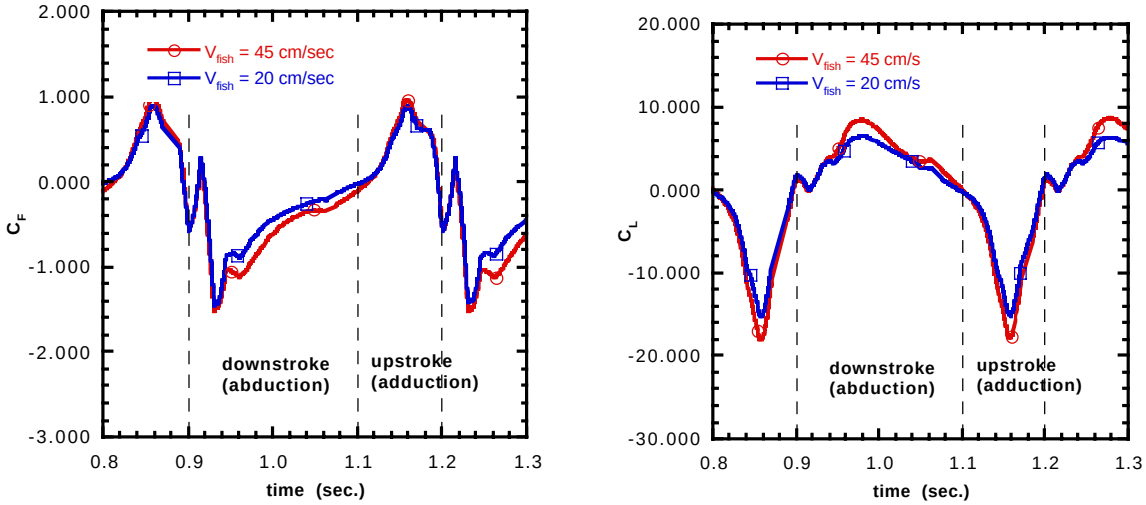

a. coefficient of thrust

b. coefficient of lift

Figure 19. Effect of swimming speed on thrust and lift coefficients for a rigid fin.